

Optimal Actuator Placement for the High-Precision Control of Quasi-Static Elastic Plates

André Heining¹, Kevin Schmidt¹, Ulrich Schönhoff, and Oliver Sawodny¹, *Senior Member, IEEE*

Abstract—Adaptive optical elements are often used to compensate for disturbances in the beam to enhance the image quality. If the element is thin, the force profile for its motion may lead to a significant unevenness of the optical surface impairing the image quality. A remedy falls back on the overactuation with a larger number of actuators. However, the question arises of what the minimal number of actuators for a given optical requirement is. Thus, we investigate the case of a low-frequency reference acceleration in the spatial degrees of freedom of a rigid body, where the elastic modes of a thin plate experience quasi-static amplification. Considering the information on the elastic plate modes, an optimal mapping of the demanded reference acceleration on the actuators leading to a minimal surface deviation from ideally flat is derived analytically. Furthermore, this mapping and the information of the nonsquare relative gain array (RGA) are exploited to obtain an actuator placement to further reduce the elastic plate deformation. Numerical results show a major improvement in flattening the optical surface profile compared to the case of neglecting the information about the elastic plate modes and lead to a Pareto front that supports the choice of a minimal number of actuators.

Index Terms—Actuator placement, distributed parameter system, feedforward control, plate vibration.

I. INTRODUCTION

THE active control of optical elements presents a common strategy to compensate for aberrations in the optical path. Recent development in optical applications considers an increasing size of the optical surface to improve the image quality [6], [11], [22]. However, maintaining the mass while increasing the surface requires a reduction of its thickness, leading to thin plates. In adaptive optics, thin elements are typically controlled by a large number of actuators to compensate for wavefront disturbances, which perturb the transmitted information and limit the image resolution in large telescopes [1], or the maximum output power of high-power lasers [21]. Considering a thin optical element that corrects for piston and tip-tilt disturbances, the force profile for its motion may lead to

Manuscript received 29 April 2022; revised 14 May 2022 and 21 April 2023; accepted 2 May 2023. Date of publication 17 July 2023; date of current version 23 October 2023. Recommended by Associate Editor T. Oomen. (Corresponding author: André Heining.)

André Heining, Kevin Schmidt, and Oliver Sawodny are with the Institute for System Dynamics, University of Stuttgart, 70563 Stuttgart, Germany (e-mail: heining@isys.uni-stuttgart.de; schmidt@isys.uni-stuttgart.de; sawodny@isys.uni-stuttgart.de).

Ulrich Schönhoff is with Carl Zeiss SMT GmbH, 73447 Oberkochen, Germany (e-mail: ulrich.schoenhoff@zeiss.com).

Color versions of one or more figures in this article are available at <https://doi.org/10.1109/TCST.2023.3291129>.

Digital Object Identifier 10.1109/TCST.2023.3291129

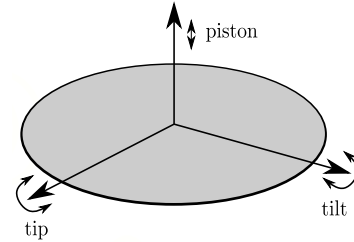


Fig. 1. Visualization of vertical piston and rotational tip-tilt motion.

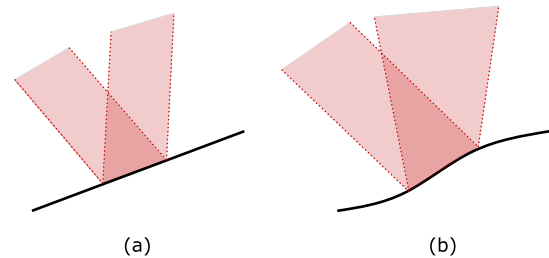


Fig. 2. Reflection of light beam on (a) ideally stiff plate and (b) elastically deformed plate.

an uneven optical surface. The surface deviation then impairs the compensation of the piston and tip-tilt disturbances and introduces additional distortions in the optical path, as shown in Figs. 1 and 2. If a high-precision control with large bandwidth is desired, the change in the surface profile needs to be kept small. In the case of a low-frequency change of the plate motion, i.e., a negligible transient system response, the applied force profile introduces a quasi-static excitation of the elastic plate modes. Common measures to compensate for the elastic plate deformation are the actuation of the plate and the positioning of actuators.

Optimal actuator placement is a frequently addressed objective in the control of dynamic systems. It has a major impact on the control performance. Moreover, the identification of optimal actuator locations is encountered repeatedly in the design process since it is coupled to the actuator force profile. Solving the coupled objectives requires an efficient optimization algorithm. Although coupled, the optimization problem can be drastically simplified by obtaining an analytic solution for the actuator force profile assuming a given actuator configuration. This leaves the positioning as an optimization problem, which can be solved by considering a state-space representation of the system for example, enabling the treatment of various complex geometries. Due to the multitude of systems and

control objectives, there is no general procedure to obtain an ideal actuator placement as shown in the following.

A. State-of-the-Art

Screening present literature shows that there are frequently addressed approaches for optimizing the system configuration. The list ranges from methods in the time domain to methods in the frequency domain. Considering the time domain, an objective based on the controllability Gramian is often minimized subject to additional constraints. Alternatively, the frequency domain offers methods such as the relative gain array (RGA), to obtain configurations that satisfy the desired conditions and is especially useful in systems with a finite amount of possible inputs and outputs.

The work of [9] gives a brief overview of typical optimization criteria. The list ranges from maximizing modal forces and the deflection of the considered structure to maximizing the controllability and observability and minimizing spillover effects that might occur when neglecting higher order modes.

Findings in [7] show the effect of piezoelectric patch-type actuators on exciting specific modes of a thin rectangular plate. Experiments give evidence that a mode is dominantly excited, if the input frequency is close to the resonant frequency of a mode. Furthermore, the location and orientation of the actuator patch play a key role in the ability to excite specific modes since the actuator edges act in phase and, thus, parallel edges are likely to support or cancel out each other in the case of the excitation of a particular mode.

Sadri et al. [20] considered two objectives for finding optimal actuator locations for active vibration control of a rectangular isotropic simply supported plate. For a fixed number of actuators, the placement obtained by maximizing the modal controllability and the controllability Gramian is compared. Simulations show the capability of both objectives to find ideal actuator locations, with the modal controllability criterion leading to slightly better damping for particular modes. The optimization problems were solved with a genetic algorithm.

In a comparable manner, the work in [17] also considers maximizing the controllability Gramian to search for an optimal configuration of piezoelectric patch actuators on a plate. Equivalently to [20], the optimization is solved with a genetic algorithm. Based on the resulting locations, an adaptive control law is synthesized to suppress the vibration response of the plate. Conducted simulations show that the optimal actuator locations improve the power efficiency of the actuators as well as the control efficiency.

An optimization of a collocated piezoelectric actuator–sensor pair is also the topic in [15]. Optimal locations are determined by solving a zero-one optimization problem by minimizing the linear quadratic regulator (LQR) performance with a genetic algorithm. The control performance of the LQR is compared to proportional feedback and negative velocity feedback. A comparison reveals a major improvement for the LQR and the negative velocity feedback and a reduction in the actuator voltages for the LQR.

Another approach considers the controllability Gramian to obtain optimal actuator placements again [16]. The objective

represents the input energy of the actuators in conjunction with an LQR. Furthermore, the number of actuators and the possible actuator locations are fixed. Therefore, the problem is solved using an integer-coded genetic algorithm.

The work of [18] considers a zero-one optimization problem for finding the optimal combination of discrete actuator locations. The problem is solved by utilizing a genetic algorithm and the cost function maximizes the dissipated energy of the controller.

Solving a zero-one optimization problem as well, Huang et al. [12] used an adaptive genetic algorithm to minimize the effort of an LQR on damping vibrations. The considered system is a thin cantilever plate and the actuators are piezoelectric patches collocated with a sensor. Results are tested in a simulation and show a major improvement in damping the plate vibration.

Chhabra et al. [4] used a modified heuristic genetic algorithm for determining the optimal location of piezoelectric actuators for the damping of plate structures. The cost function maximizes the singular value of a modified control matrix. Findings show that the modified algorithm converges to the global optimum and optimized placements together with an LQR lead to a significant increase in the closed-loop damping ratio.

In addition to the dynamic view on a system, the compensation of stationary effects is approached as well. Therefore, optimal actuator locations for compensating static disturbances by controlling the shape are obtained in [10]. The root mean square (rms) defines the objective and the optimization problem is solved by using the NEWSUMT package. The optimization scheme is applicable to the placement of force and heat actuators and was applied to a beam.

Furthermore, Wagner et al. [28] investigated the actuator placement on a 1-D Euler–Bernoulli beam to counteract static loads. In order to obtain the ideal positions for a given number of actuators, the trace of the Gramian compensability matrix is minimized.

Besides the optimization of the actuator placement via Gramian matrices, the coupling between the input and output of a system in a steady state is often of interest. The RGA presents a mature technology for systems with multiple-input–multiple-output (MIMO) to assess this kind of coupling. The RGA for square systems was first introduced by Bristol [2] and transferred to nonsquare systems with multiple inputs and outputs by Cheng and Yu [3].

For example, a multivariable control scheme for a ternary distillation column is designed by the use of the RGA [26]. Therefore, the nonsquare system is first transformed into a squared one by applying a precompensation matrix.

A second application controls the de-oiling membrane process [14]. Based on the evaluation of the RGA, the decoupling of control loops was improved and it turned out that actuators need to be located differently depending on the operating point.

Moreover, the bending vibration of a cantilever plate was analyzed by an extension to the RGA in [8]. By the use of a

block RGA (BRG), the actuator location for two sets of three self-sensing actuators is determined.

More recently, the temperature of a walking beam furnace was subject of control in [13]. However, the application of the RGA did not lead to a sufficient control performance and, thus, was replaced by a Gramian interaction measure.

B. Contribution and Structure of This Article

The correction for piston and tip-tilt disturbances requires the realization of a demanded motion. This shall be done without introducing additional distortions of an uneven optical surface through the applied force profile. Moreover, it is desirable to realize this with a low number of actuators. Hence, the contribution of this article is twofold:

- 1) an analytically derived expression for the actuator force profile that realizes the demanded motion and assures a minimal surface deflection under the assumption of a quasi-static response of the elastic plate modes;
- 2) a procedure for obtaining optimized actuator locations by considering the results of 1) and aspects from the time and frequency domains leading to a Pareto front for deciding on the number of actuators.

Therefore, the remaining article is structured as follows. In Section II, the underlying model for the optimization procedure is derived. Hereinafter, we present an analytic solution of the optimal mapping of the desired rigid body acceleration on the actuator force profile by taking information of the elastic plate modes into account. Advancing from here, a procedure for obtaining optimized actuator locations by combining methods from the time and frequency domains is additionally covered in Section III. Subsequently, the discussion in Section IV presents the numerical results for a low number of actuators and an analysis of the plate deformation for a given rigid body acceleration. Moreover, gathering the results for the different amounts of actuators leads to a Pareto front that serves as a tool on selecting the minimal amount of actuators. A summary and outlook concludes this article with Section V.

II. MODELING

In this section, the governing equations for a circular plate with elastic boundary are presented. Subsequently, the quasi-stationary model in the case of a slowly varying rigid body acceleration is derived.

A. System Modeling

A truncated design model, which is partitioned in the rigid body modes (subscript r) and elastic modes (subscript e), is the basis for the further steps of this article and is given as

$$\frac{d}{dt} \begin{bmatrix} \mathbf{x}_r \\ \mathbf{x}_e \end{bmatrix} = \begin{bmatrix} \mathbf{A}_r & \\ & \mathbf{A}_e \end{bmatrix} \begin{bmatrix} \mathbf{x}_r \\ \mathbf{x}_e \end{bmatrix} + \begin{bmatrix} \mathbf{B}_r \\ \mathbf{B}_e \end{bmatrix} \mathbf{u} \triangleq \mathbf{A}\mathbf{x} + \mathbf{B}\mathbf{u}. \quad (1)$$

The considered rigid body degrees of freedom (DoFs) cover a piston and tip-tilt motion (see Fig. 1). However, the state-space description can be easily extended by the remaining three DoFs. For a wide range of mechatronic applications, it is sufficient to consider a circular region of interest—at least

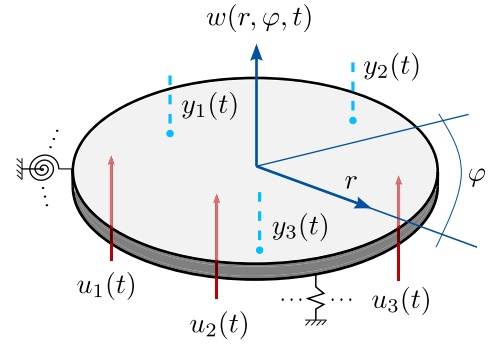


Fig. 3. Model of thin plate with $u_i(t)$ and $i \in \mathbb{N}$ as the force input as well as $y_j(t)$ and $j \in \mathbb{N}$ as measured plate deflection perpendicular to its surface and elastic boundary support.

for fundamental design issues like an optimal placement of the actuators. Thus, we introduce a dynamic thin-plate model in the following (see Fig. 3). In this case, the elastic support represents the stiffness of the remaining geometry outside the region of interest.

1) *Dynamic Thin-Plate Model:* In order to illustrate the proposed actuator placement methodology, we consider a circular region of interest of a Kirchhoff plate with radius R and thickness h in polar coordinates (r, φ) . For any time $t > 0$ and $(r, \varphi) \in (0, R) \times (0, 2\pi)$, the deflection $w(r, \varphi, t)$ is governed by the partial differential equation (PDE)

$$D\Delta\Delta w + \rho h \frac{\partial^2 w}{\partial t^2} + Q_d = Q_a \quad (2)$$

depending on the fundamental material parameters E modulus of elasticity, ν Poisson's ratio, ρ the mass density, and the flexural rigidity $D = Eh^3/(12[1 - \nu^2])$. The spatial Laplace operator in polar coordinates is denoted $\Delta = \partial_r^2 + \partial_r/r + \partial_\varphi^2/r^2$. Moreover, a Rayleigh damping force is considered

$$Q_d(r, \varphi, t) = \lambda_d \frac{\partial w(r, \varphi, t)}{\partial t} + \kappa_d \Delta \Delta \frac{\partial w(r, \varphi, t)}{\partial t} \quad (3)$$

featuring a viscous and a Kelvin–Voigt component with the coefficients λ_d and κ_d , respectively. The plate is actuated by $i = 1, \dots, m_a$ pointwise force actuators $u_i(t)$ at the polar positions $(r_{a,i}, \varphi_{a,i})$, which are collected within the expression

$$Q_a(r, \varphi, t) = \sum_{i=1}^{m_a} \frac{u_i(t)}{r_{a,i}} \delta(r - r_{a,i}) \delta(\varphi - \varphi_{a,i}) \quad (4)$$

where $\delta(\cdot)$ is the Dirac delta distribution. Note that the actuator locations and the number of actuators m_a are design variables in the remainder of this article.

As the system equations are linear, we assume homogeneous initial conditions $w(r, \varphi, 0) = \partial_t w(r, \varphi, 0) = 0$ without any loss of generality and ∂_t as the partial derivative of w with respect to t . In order to define the boundary conditions at $r = R$ properly, consider the operators

$$\mathcal{M} = -D \left[\frac{\partial^2}{\partial r^2} + \frac{\nu}{r} \frac{\partial}{\partial r} + \frac{\nu}{r^2} \frac{\partial^2}{\partial \varphi^2} \right] \quad (5)$$

$$\mathcal{V} = -D \left[\Delta \frac{\partial}{\partial r} + \frac{1-\nu}{r} \frac{\partial^2}{\partial \varphi^2} \left(\frac{1}{r} \frac{\partial}{\partial r} - \frac{1}{r^2} \right) \right] \quad (6)$$

which correspond to the boundary bending moment $\mathcal{M}w$ and the Kelvin–Kirchhoff shearing force $\mathcal{V}w$, respectively [24], [29]. With the preliminary definition, the boundary conditions read as

$$\mathcal{M}w(R, \varphi, t) = c_{\mathcal{M}} \frac{\partial w(R, \varphi, t)}{\partial r} \quad (7)$$

$$\mathcal{V}w(R, \varphi, t) = -c_{\mathcal{V}} w(R, \varphi, t) \quad (8)$$

with the rotational and translational stiffness functions $c_{\mathcal{M}}$ and $c_{\mathcal{V}}$, respectively.

2) *Modal Analysis and Truncation:* For an analysis of the plate deflection, the deflection $w(r, \varphi, t)$ is decomposed in spatially dispersed plate modes $\psi_{mn}(r, \varphi)$ and time-dependent modal amplitudes $q_{mn}(t)$. The index $m \in \mathbb{N}_+$ denotes the number of concentric nodal lines and the index $n \in \mathbb{N}_+$ represents radial nodal lines in the elastic modes [29]. In accordance with the preceding one, the modal analysis is performed by applying the modal transformation

$$q_{mn}(t) = \iint_{\mathcal{P}} w(r, \varphi, t) \psi_{mn}(r, \varphi) r dr d\varphi \quad (9)$$

to the PDE (2), with the plate area $\mathcal{P} = (0, R) \times (0, 2\pi)$. By performing integration by parts twice and applying Green's theorem, we obtain the following eigenvalue problem with the corresponding eigenvalues λ_{mn} :

$$\Delta \Delta \psi_{mn}(r, \varphi) - \frac{\lambda_{mn}^4}{R^4} \psi_{mn}(r, \varphi) = 0, \quad (r, \varphi) \in \mathcal{P} \quad (10)$$

and the boundary conditions

$$\mathcal{M}\psi_{mn}(R, \varphi) = c_{\mathcal{M}} \frac{\partial \psi_{mn}(R, \varphi)}{\partial r} \quad (11a)$$

$$\mathcal{V}\psi_{mn}(R, \varphi) = -c_{\mathcal{V}} \psi_{mn}(R, \varphi). \quad (11b)$$

By performing a multiplicative separation of the operator in (10), the expression is rewritten as

$$\left(\Delta - \frac{\lambda_{mn}^2}{R^2} \right) \left(\Delta + \frac{\lambda_{mn}^2}{R^2} \right) \psi_{mn}(r, \varphi) = 0 \quad (12)$$

leading to two independent solution parts

$$\left(\Delta - \frac{\lambda_{mn}^2}{R^2} \right) \Psi_{1,mn}(r, \varphi) = 0 \quad (13a)$$

$$\left(\Delta + \frac{\lambda_{mn}^2}{R^2} \right) \Psi_{2,mn}(r, \varphi) = 0 \quad (13b)$$

that add up to the overall solution

$$\psi_{mn}(r, \varphi) = \Psi_{1,mn}(r, \varphi) + \Psi_{2,mn}(r, \varphi). \quad (14)$$

With some further calculus, the independent solution parts are reshaped to Bessel's ordinary differential equation (ODE), and thus, the solution approach for the plate modes $\psi_{mn}(r, \varphi)$ is formed by superpositioning the Bessel functions of the first and second kinds, i.e., $J_n(\cdot)$ and $Y_n(\cdot)$, respectively, and the modified Bessel functions of the first and second kinds, i.e., $I_m(\cdot)$ and $K_m(\cdot)$, respectively. Hence,

$$\begin{aligned} \psi_{mn}(r, \varphi) = & A_{mn} \left[J_n \left(\frac{\lambda_{mn} r}{R} \right) + B_{mn} Y_n \left(\frac{\lambda_{mn} r}{R} \right) \right. \\ & \left. + C_{mn} I_m \left(\frac{\lambda_{mn} r}{R} \right) + D_{mn} K_m \left(\frac{\lambda_{mn} r}{R} \right) \right] e^{-im\varphi} \end{aligned} \quad (15)$$

forms the solution for the plate modes. The normalization factor A_{mn} and the shape parameters B_{mn} , C_{mn} , and D_{mn} are determined by solving the boundary conditions (11) and further demanding

$$\lim_{r \rightarrow 0} \psi_{mn}(r, \varphi) < \infty \quad (16)$$

$$\psi_{mn}(r, 0) = \psi_{mn}(r, 2\pi). \quad (17)$$

The demand of (16) enforces the coefficients B_{mn} and D_{mn} to vanish since the Bessel function of the second kind and the modified function of the second kind exhibit a singularity at $r = 0$. Plugging (15) into the boundary conditions (11a) and (11b) and further eliminating the remaining shape parameter C_{mn} leads to the frequency equation whose roots define the values of λ_{mn} [29]. The condition for determining the normalization factor A_{mn} is then given by

$$\int_0^{2\pi} \int_0^R \psi_{mn}(r, \varphi) \psi_{pq}(r, \varphi) r dr d\varphi = \delta_{mp} \delta_{nq} \quad (18)$$

with $\delta_{ab} = 1$ for $a = b$ and zero elsewhere. Thus, the normalization factor is defined with

$$A_{mn} = \left(\int_0^{2\pi} \int_0^R \left(\left(J_n \left(\frac{\lambda_{mn} r}{R} \right) + C_{mn} I_n \left(\frac{\lambda_{mn} r}{R} \right) \right) \cos(n\varphi) \right)^2 r dr d\varphi \right)^{-\frac{1}{2}}. \quad (19)$$

Moreover, the decoupled ODEs

$$\begin{aligned} \ddot{q}_{mn}(t) + 2\zeta_{mn}\omega_{mn}\dot{q}_{mn}(t) + \omega_{mn}^2 q_{mn}(t) \\ = \sum_{i=1}^{m_a} \frac{\psi_{mn}(r_{a,i}, \varphi_{a,i})}{\rho h r_{a,i}} u_i(t), \quad t > 0 \end{aligned} \quad (20)$$

describe the dynamics of the modal amplitudes $q_{mn}(t)$, with resonance frequency

$$\omega_{mn}^2 = \frac{D\lambda_{mn}^4}{\rho h R^4}$$

damping coefficient

$$\zeta_{mn} = \frac{\lambda_d R^4 + \kappa_d \lambda_{mn}^4}{2\rho h R^4 \omega_{mn}}$$

and the initial condition $q_{mn}(0) = \dot{q}_{mn}(0) = 0$. The original plate deflection is then obtained by an infinite series of the real-valued plate modes, i.e.,

$$w(r, \varphi, t) = \text{Re} \sum_{m,n=0}^{\infty} \psi_{mn}(r, \varphi) q_{mn}(t). \quad (21)$$

However, for a practical application, only a finite number of plate modes can be considered, leading to

$$w(r, \varphi, t) \approx \text{Re} \sum_{m,n=0}^{N_m, N_n} \psi_{mn}(r, \varphi) q_{mn}(t) \quad (22)$$

with N_n and N_m as the bounds on the considered plate modes. Similarly, the truncated design model (1) is obtained by gathering a finite amount of modal amplitudes $q_{mn}(t)$ and their first time derivative $\dot{q}_{mn}(t)$ in the state vectors \mathbf{x}_r and \mathbf{x}_e .

B. Quasi-Stationary Model

In order to formulate the quasi-static problem description, further conditions on the system equations (1) are proposed.

The modal state vector \mathbf{x} is structured as

$$\begin{aligned}\mathbf{x} &= (\mathbf{x}_1^\top \cdots \mathbf{x}_k^\top \cdots \mathbf{x}_{n_m}^\top)^\top \\ \mathbf{x}_k &= (q_k \dot{q}_k)^\top \\ k &\in \{1, \dots, n_m\}\end{aligned}$$

where n_m denotes the number of considered modes sorted in ascending natural frequency.

Under the assumption of constant rigid body acceleration and identically zero elastic mode velocity, i.e.,

$$\ddot{\mathbf{q}}_r = \text{const.} \Rightarrow \dot{\mathbf{x}}_r \neq \mathbf{0} \quad (23a)$$

$$\ddot{\mathbf{q}}_e = \dot{\mathbf{q}}_e = \mathbf{0} \Rightarrow \dot{\mathbf{x}}_e = \mathbf{0} \quad (23b)$$

the remaining system equations that constitute the quasi-static case are

$$\mathbf{0} = \mathbf{A}_e \mathbf{x}_e + \mathbf{B}_e \mathbf{u} \quad (24a)$$

$$\ddot{\mathbf{q}}_r = \bar{\mathbf{B}}_r \mathbf{u} \quad (24b)$$

with $\bar{\mathbf{B}}_r = (\mathbf{I} \otimes [0 \ 1]) \mathbf{B}_r$ and \otimes denoting the Kronecker product.

III. ACTUATOR FORCE PROFILE AND PLACEMENT

This section treats the mapping of the demanded acceleration $\ddot{\mathbf{q}}_r$ on the force profile of the actuators for a given configuration. First, the simplified case in which the information about the elastic states of the plate is neglected, called “naive” approach, is derived, and in a second step, the optimal mapping that minimizes the plate deflection for a given acceleration and actuator configuration is presented. Hereinafter, we describe a procedure for obtaining actuator positions that minimizes the worst case deflection by exploiting the optimal mapping and the information from the RGA.

A. Actuator Force Profile

A naive approach to calculate an actuator force profile that satisfies the desired rigid body acceleration neglects the quasi-static plate deflection of the elastic modes. Hence, solving the optimization problem

$$\min_{\mathbf{u}} \frac{1}{2} \mathbf{u}^\top \mathbf{u} \quad (25a)$$

$$\text{s.t. } \mathbf{a} = \mathbf{W} \bar{\mathbf{B}}_r \mathbf{u} \quad (25b)$$

leads to a minimal force profile that accounts for the desired acceleration \mathbf{a} , with $\mathbf{W} = \mathbf{W}^\top > 0$ denoting the scaling matrix between the desired rigid body acceleration and the acceleration of the rigid body modes \mathbf{q}_r . Appendix II provides a detailed derivation for the scaling matrix \mathbf{W} that is considered in this article. The obtained input profile is defined by

$$\mathbf{u}_{\text{naive}}^* = \bar{\mathbf{B}}_r^+ \mathbf{W}^{-1} \mathbf{a} \quad (26)$$

whereby the operator $[\cdot]^+$ denotes the Moore–Penrose pseudoinverse. However, this definition of the actuator’s force profile ignores the plate deformation that is imposed by the

elastic plate modes \mathbf{q}_e that are equally excited by the actuator action. Thus, the resulting force profile may lead to large quasi-static plate deformations.

The new approach that is pursued here aims for a force profile of the attached actuators that minimizes the quasi-static plate deformation subject to the satisfaction of the desired rigid body acceleration. This requirement is captured by

$$\min_{\mathbf{u}} \|w(r, \varphi)\|_{L_2}^2 \quad (27a)$$

$$\text{s.t. } \mathbf{a} = \mathbf{W} \bar{\mathbf{B}}_r \mathbf{u}. \quad (27b)$$

Next, the plate deformation is expressed by the modal synthesis

$$w(r, \varphi) = \boldsymbol{\psi}^\top(r, \varphi) \mathbf{x}_e = \boldsymbol{\psi}^\top(r, \varphi) \mathbf{A}_e^{-1} \mathbf{B}_e \mathbf{u}. \quad (28)$$

This leads to the reformulation of the objective to

$$\begin{aligned}\|w(r, \varphi)\|_{L_2}^2 &= \iint_{\mathcal{P}} w^2(r, \varphi) r dr d\varphi \\ &= \mathbf{u}^\top \mathbf{B}_e^\top (\mathbf{A}_e^{-1})^\top \underbrace{\iint_{\mathcal{P}} \boldsymbol{\psi} \boldsymbol{\psi}^\top r dr d\varphi}_{=\mathbf{I}} \mathbf{A}_e^{-1} \mathbf{B}_e \mathbf{u} \\ &= \frac{1}{2} \mathbf{u}^\top \mathbf{H} \mathbf{u}. \quad (29)\end{aligned}$$

Note that the eigen shapes $\boldsymbol{\psi}$ are self-adjoint and, hence, form an orthonormal basis system; their product equals the identity matrix \mathbf{I} . Moreover, due to the symmetric structure of \mathbf{H} , the matrix is positive definite, i.e., $\mathbf{H} > 0$, and Gramian. The aforementioned reformulation leads to

$$\min_{\mathbf{u}} \frac{1}{2} \mathbf{u}^\top \mathbf{H} \mathbf{u} \quad (30a)$$

$$\text{s.t. } \mathbf{a} = \mathbf{W} \bar{\mathbf{B}}_r \mathbf{u}. \quad (30b)$$

By formulating the Lagrangian

$$\mathcal{L}(\mathbf{u}, \boldsymbol{\lambda}) = \frac{1}{2} \mathbf{u}^\top \mathbf{H} \mathbf{u} + \boldsymbol{\lambda}^\top (\mathbf{W} \bar{\mathbf{B}}_r \mathbf{u} - \mathbf{a}) \quad (31)$$

with $\boldsymbol{\lambda}$ as the Lagrange multiplier for the equality constraint, and calculating the partial derivatives with respect to the arguments of the Lagrangian

$$\frac{\partial \mathcal{L}}{\partial \mathbf{u}} = \mathbf{H} \mathbf{u} + (\mathbf{W} \bar{\mathbf{B}}_r)^\top \boldsymbol{\lambda} = \mathbf{0} \quad (32a)$$

$$\frac{\partial \mathcal{L}}{\partial \boldsymbol{\lambda}} = \mathbf{W} \bar{\mathbf{B}}_r \mathbf{u} - \mathbf{a} = \mathbf{0} \quad (32b)$$

we obtain the following system of linear equations:

$$\begin{pmatrix} \mathbf{H} & (\mathbf{W} \bar{\mathbf{B}}_r)^\top \\ \mathbf{W} \bar{\mathbf{B}}_r & \mathbf{0} \end{pmatrix} \begin{pmatrix} \mathbf{u} \\ \boldsymbol{\lambda} \end{pmatrix} = \begin{pmatrix} \mathbf{0} \\ \mathbf{a} \end{pmatrix}. \quad (33)$$

Solving for the arguments \mathbf{u} and $\boldsymbol{\lambda}$ leads to

$$\boldsymbol{\lambda} = -(\mathbf{W} \bar{\mathbf{B}}_r \mathbf{H}^{-1} \bar{\mathbf{B}}_r)^\top \mathbf{a} \quad (34a)$$

$$\mathbf{u} = -\mathbf{H}^{-1} \bar{\mathbf{B}}_r^\top \mathbf{W} \boldsymbol{\lambda}. \quad (34b)$$

By combining (34a) and (34b), we conclude

$$\mathbf{u} = \mathbf{H}^{-1} \bar{\mathbf{B}}_r^\top \mathbf{W} (\mathbf{W} \bar{\mathbf{B}}_r \mathbf{H}^{-1} \bar{\mathbf{B}}_r)^\top \mathbf{a} \triangleq \mathbf{K}_{\text{FF}} \mathbf{a}. \quad (35)$$

Here, the matrix \mathbf{K}_{FF} describes a mapping of the desired rigid body acceleration on the force profile of the actuators such that the plate deformation is kept small. However, the optimization of the quasi-static deformation profile can be pushed another step further.

B. Optimization of Actuator Configuration

Up until now, only given actuator positions were considered. Thus, by optimizing the actuator placement, the plate deformation may be reduced even further. In order to prepare an optimization over the actuator positions, the optimization variable $\theta \in \mathbb{R}^{f m_a}$, with f as the DoF of each actuator and m_a denoting the number of actuators, needs to be declared. In our case, we consider actuators with two DoFs comprising the polar coordinates $(r_{a,i}, \varphi_{a,i})$ of their position. Hence, θ is structured as

$$\theta = (r_{a,1} \ \varphi_{a,1} \ \cdots \ r_{a,m_a} \ \varphi_{a,m_a})^\top \in \mathbb{R}^{2m_a}. \quad (36)$$

In the next step, the matrices that depend on the actuator position have to be identified. From the PDE (2), it is obvious that only the input matrices $B_r = B_r(\theta)$ and $B_e = B_e(\theta)$ depend on the actuator position. However, the matrices K_{FF} and H depend on the input matrices B_r and B_e and, thus, implicitly depend on the actuator positions as well.

1) *Worst Case Optimization:* The goal of the optimization over the actuator positions is to determine an actuator configuration that minimizes the quasi-static plate deformation for an arbitrary rigid body acceleration. Thus, the optimal mapping of \mathbf{a} onto \mathbf{u} is inserted in the squared L_2 -norm of the plate deformation profile, leading to

$$\begin{aligned} \|w(r, \varphi)\|_{L_2}^2 &= \frac{1}{2} \mathbf{a}^\top \mathbf{K}^\top(\theta) \mathbf{H}(\theta) \mathbf{K}(\theta) \mathbf{a} \\ &= \frac{1}{2} \mathbf{a}^\top \mathbf{Q}(\theta) \mathbf{a}. \end{aligned} \quad (37)$$

Since the Gramian matrix \mathbf{H} is left and right multiplied by \mathbf{K}^\top and \mathbf{K} , respectively, the expression $\mathbf{Q}(\theta)$ is Gramian as well. Moreover, the demanded rigid body acceleration \mathbf{a} is in general not constant and may vary in successive plate motions. Therefore, it is intended to find an actuator configuration that minimizes the imposed plate deformation of arbitrary accelerations \mathbf{a} . By exploiting the fact that $\mathbf{Q}(\theta)$ is Gramian, it can be lower and upper bounded by its smallest and largest eigenvalues λ_{\min} and λ_{\max} , respectively, i.e.,

$$\frac{1}{2} \lambda_{\min}(\mathbf{Q}(\theta)) \|\mathbf{a}\|^2 \leq \frac{1}{2} \mathbf{a}^\top \mathbf{Q}(\theta) \mathbf{a} \leq \frac{1}{2} \lambda_{\max}(\mathbf{Q}(\theta)) \|\mathbf{a}\|^2. \quad (38)$$

As a consequence, minimizing the largest eigenvalue $\lambda_{\max}(\theta)$ returns a placement of the actuators that minimizes the quasi-static deformation profile $w(r, \varphi)$ caused by the acceleration \mathbf{a} . For a better understanding, this problem might be interpreted geometrically. The matrix $\mathbf{Q}(\theta) \in \mathbb{R}^{n \times n}$ represents an n -dimensional ellipsoid whose semiaxes are proportional to the eigenvalues of $\mathbf{Q}(\theta)$. By a left and right multiplication of the vector $\mathbf{a} \in \mathbb{R}^n$, the vector is projected onto the ellipsoid. The largest projection occurs in the direction of the largest semiaxis. Hence, for minimizing the largest projection, the eccentricity of the ellipsoid needs to be reduced, which is equivalent to minimizing the largest eigenvalue of $\mathbf{Q}(\theta)$. The geometric interpretation is shown in Fig. 4 for the dimension $n = 2$.

Since no further constraints on the input \mathbf{u} have to be considered, only the distance between the single actuator locations has to be greater or equal to a minimal distance

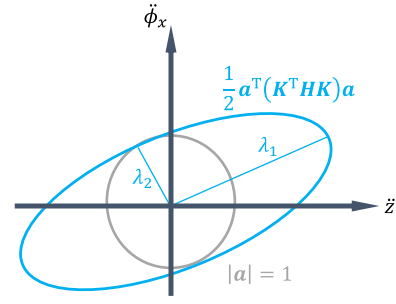


Fig. 4. Geometric explanation of projection on ellipsoid for two dimensions.

in order to ensure a realizable configuration. Therefore, worst case minimization of the influence of the acceleration \mathbf{a} on the quasi-static plate deformation is represented by

$$\min_{\theta} \max \lambda(\mathbf{Q}(\theta)) \quad (39a)$$

$$\text{s.t. } d_{\min}(\theta) \geq d_{\text{crit}} \quad (39b)$$

$$(r_{a,i}, \varphi_{a,i}) \in \tilde{\mathcal{P}} \quad (39c)$$

with $\tilde{\mathcal{P}} \subseteq \mathcal{P}$ as subset of the feasible plate area. However, due to the nonlinear dependence of the eigenvalues on the polar coordinates, the optimization over the actuator locations forms a nonlinear and nonconvex optimization problem. The difficulty of nonconvex optimizations is the presence of multiple local minima. These local minima may result in a solution that contains a local gathering of actuators. In order to enforce a distribution of the actuators over the plate, the nonsquare RGA (NS-RGA) is considered as an additional aspect in the optimization.

2) *Nonsquare Relative Gain Array:* The NS-RGA is defined as

$$\Lambda(s) = \mathbf{G}(s) \circ (\mathbf{G}(s)^+)^{\top} \in \mathbb{R}^{m_o \times m_i} \quad (40)$$

with $\mathbf{G}(s)$ as the transfer function matrix from the considered m_i inputs to the desired m_o outputs and the operator \circ denoting the Hadamard product [3]. The element $\Lambda_{j,i}$ describes the interaction of the i th input to the j th output. Some important properties of the NS-RGA are given as follows.

$$1) \text{ The sum of each column equals 1, } c_{\Sigma,i} = \sum_{j=1}^{m_o} \Lambda_{j,i} = 1 \ \forall i \in 1, \dots, m_i.$$

$$2) \text{ The sum of each row lies in between 0 and 1, } 0 \leq r_{\Sigma,j} = \sum_{i=1}^{m_i} \Lambda_{j,i} \leq 1 \ \forall j \in 1, \dots, m_o.$$

In particular, the second property forms a key aspect for the considered optimization. Therefore, we introduce an adapted input matrix

$$\tilde{\mathbf{B}}_e(\theta) = \mathbf{B}_e(\theta) \mathbf{K}_{FF}(\theta) \quad (41)$$

considering the rigid body acceleration as the new system input. Moreover, the output matrix \mathbf{C}_e is set up by m_o point measurements of the local plate deviation from its middle line to obtain a transfer function matrix of finite dimension. The locations of the system outputs are calculated by the utilization of a planar Fibonacci grid (see Fig. 5), which presents a simple solution for a virtually uniformly distributed set of points [23]. This yields the transfer function matrix from the desired rigid body acceleration \mathbf{a} to the defined system output \mathbf{y}

$$\mathbf{G}_{y\mathbf{a}}(s, \theta) = \mathbf{C}_e (\mathbf{I}s - \mathbf{A}_e)^{-1} \tilde{\mathbf{B}}_e(\theta). \quad (42)$$

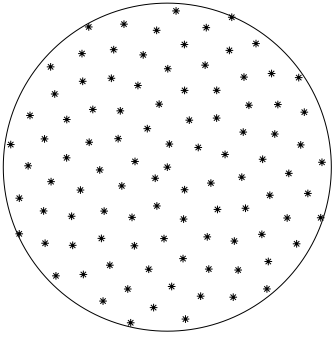


Fig. 5. Visualization of a Fibonacci grid over a circular area with 100 points.

By evaluating the transfer function (42) at the limit $\lim_{s \rightarrow 0} s$, the stationary NS-RGA

$$\bar{\Lambda}(\theta) = \bar{G}(\theta) \circ (\bar{G}(\theta)^+)^{\top} \quad (43)$$

with $\bar{G}(\theta) = G_{ya}(0, \theta)$, is obtained. In addition, it should be mentioned that the use of the Moore–Penrose pseudoinverse does not preserve the property of unit invariance if scaling of the input and output signals does occur as it is the case for the RGA of square systems [27]. Therefore, Uhlmann [27] introduced a generalized inverse, which preserves unit invariance through unit scaling. However, in the presented problem, no unit scaling of the inputs and outputs of $\bar{G}(\theta)$ occurs and, thus, the use of the Moore–Penrose pseudoinverse is valid. Next, the steady-state error

$$e = y_d - y \quad (44)$$

with the desired output y_d and the plant output y moves in the focus of investigation. By considering a minimal error in the sense of least squares (see Appendix I), (44) rewrites to

$$e = \left(I_{m_o} - \bar{G}(\theta) \bar{G}^+(\theta) \right) y_d. \quad (45)$$

Thus, the error of the j th output is

$$\begin{aligned} e_j &= \left(1 - \left(\bar{G}(\theta) \bar{G}^+(\theta) \right)_{jj} \right) y_{d,j} \\ &= (1 - r_{\Sigma,j}(\theta)) y_{d,j} \end{aligned} \quad (46)$$

according to [3], with $(\Xi)_{jj}$ denoting the jj -entry of Ξ .

Hence, in order to achieve an evenly distributed compensation of the elastic plate deformation, each row sum needs to be close to one. Therefore, the mean deviation of the row sums from one is minimized, i.e.,

$$\min_{\theta} \frac{\sum_{j=1}^{m_o} 1 - r_{\Sigma,j}(\theta)}{m_o} \quad (47a)$$

$$\text{s.t. } d_{\min}(\theta) \geq d_{\text{crit}} \quad (47b)$$

$$(r_{a,i}, \varphi_{a,i}) \in \tilde{\mathcal{P}}. \quad (47c)$$

3) *Optimization of Actuator Position:* Finding optimal actuator locations that lead to a minimal surface deflection induced by rigid body accelerations is done by combining both

criteria (39) and (47). This leads to

$$\min_{\theta} w_1 \max \lambda(Q(\theta)) + w_2 \frac{\sum_{j=1}^{m_o} 1 - r_{\Sigma,j}(\theta)}{m_o} \quad (48a)$$

$$\text{s. t. } d_{\min}(\theta) \geq d_{\text{crit}} \quad (48b)$$

$$(r_{a,i}, \varphi_{a,i}) \in \tilde{\mathcal{P}} \quad (48c)$$

with the weights $0 < w_{1,2} \in \mathbb{R}$ for adjusting the influence of each criteria. Furthermore, the inequality constraint is included in the cost function (48a) for a better numerical evaluation by utilizing a logarithmic barrier function, i.e.,

$$\Phi(\theta) = \begin{cases} -\log \Delta d, & \Delta d = d_{\min}(\theta) - d_{\text{crit}} \geq 0 \\ \infty, & \text{else.} \end{cases} \quad (49)$$

This finally leads to

$$\begin{aligned} \min_{\theta} w_1 \max \lambda(Q(\theta)) \\ + w_2 \frac{\sum_{j=1}^{m_o} 1 - r_{\Sigma,j}(\theta)}{m_o} + w_3 \Phi(\theta) \\ \text{s.t. } (r_{a,i}, \varphi_{a,i}) \in \tilde{\mathcal{P}} \end{aligned} \quad (50)$$

with $0 < w_3 \in \mathbb{R}$ as a third weight. The problem (50) is then solved with the genetic algorithm *ga* provided by MATLAB. Since the genetic algorithm is based on a stochastic exploration of the feasible set, the optimization is solved $0 < N \in \mathbb{N}$ times for each number of considered actuators, whereby each iteration for $N \geq 2$ is initialized by the best individual of the preceding iteration.

IV. SIMULATION RESULTS AND DISCUSSION

In the following, the effect of the optimal actuator force mapping $K_{FF}(\bar{\theta})$ for a given actuator configuration $\bar{\theta}$ and the further improvement through an optimized actuator positioning (OAP) is subject of investigation. The actuator configuration $\bar{\theta}$ is set to be evenly distributed over the plate and, thus, determined by evaluating the Fibonacci grid for $m_a = 10$ actuators. The location of the Fibonacci actuator placement (FAP) is shown in Fig. 9. Moreover, the considered rigid body acceleration is set to

$$a = a_{\max} \begin{pmatrix} 1 & -1 & 1 \end{pmatrix}^{\top}, \quad 0 < a_{\max} \in \mathbb{R}. \quad (51)$$

Furthermore, the first 26 elastic plate modes are included in the model description. The plate translation and its rotation around the plates' local x - and y -axes are considered for the rigid body modes. Moreover, the boundary stiffness c_M and c_Y are both set to zero, which leads to a free boundary, and the feasible set of actuator locations is set equal to the whole plate area, i.e., $\tilde{\mathcal{P}} = \mathcal{P}$.

A. Input Profiles and Modal Excitation

The naive solution for the actuator force profile is obtained by applying (26) to the vector a and leads to the quasi-static plate deformation shown in Fig. 6. Clearly, large deflections of the normalized deformation profile are detectable on the boundary of the plate and in its center. In contrast to that, the mapping of the rigid body acceleration via the mapping $K_{FF}(\bar{\theta})$ on the actuator profile leads to a reduced deformation

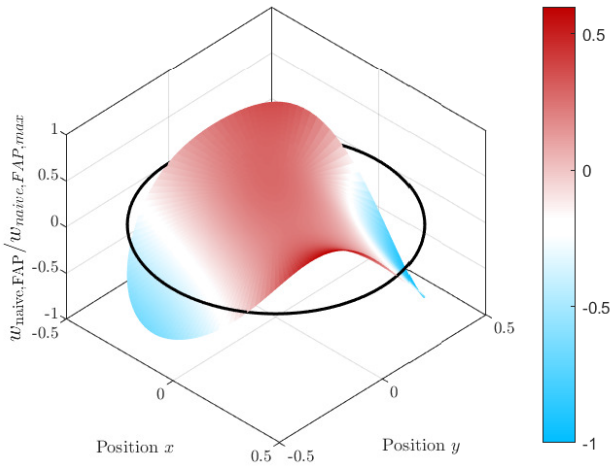


Fig. 6. Normalized plate deformation for Fibonacci grid-based actuator placement and naive force mapping via pseudoinverse with ten actuators.

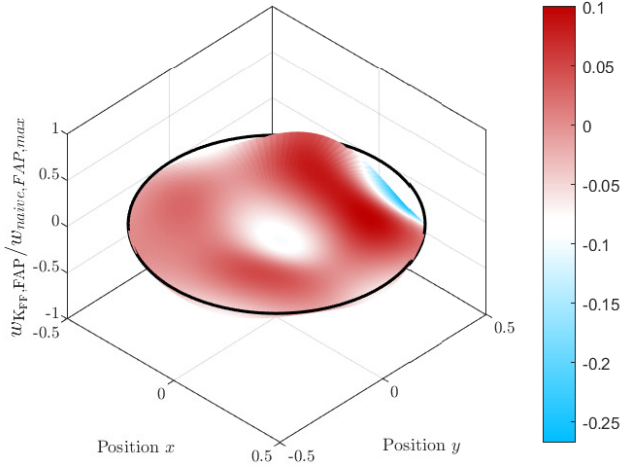


Fig. 7. Normalized plate deformation for Fibonacci grid-based actuator placement and optimal force mapping with K_{FF} for ten actuators.

as it is visible in Fig. 7. By applying the optimal mapping, the large plate deflections at the boundary and in its center are reduced and shifted to a concentric ring area on the plate. This is connected to the shifted excitation of plate modes (see Fig. 8). In the case of the naive use of the direct pseudoinverse, mainly the lower frequent plate modes are excited. These modes have a lower modal stiffness compared to the higher ordered modes and, thus, lead to a greater plate deflection, if excited. The mapping $K_{FF}(\theta)$ exploits the information about the elastic plate modes, which are gathered in the system description and shifts the excitation of the modes in the midrange of the considered model modes. In particular, the first three elastic plate modes are much less excited than in the naive case. The shift of the mode excitation through the optimal mapping leads to a peak deformation, which is reduced to 35.13% of the deformation profile in the naive case (see Table I). However, the lower third of the considered modes still experience some excitation. This indicates that there remains some potential for further improvement through an OAP.

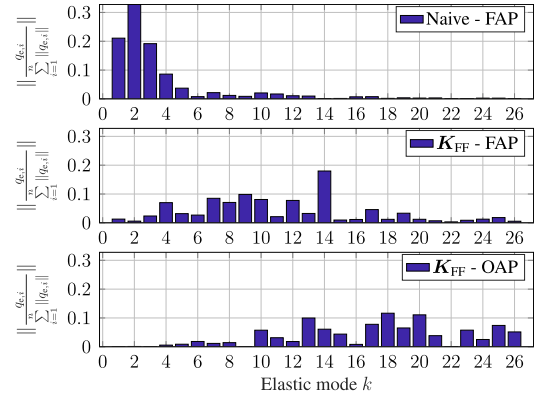


Fig. 8. Comparison between relative modal amplitude excitation with ten actuators.

TABLE I

PEAK AND RMS PLATE DEFORMATION FOR OPTIMAL ACCELERATION MAPPING WITH FAP AND OAP NORMALIZED TO PEAK AND RMS DEFORMATION OF THE NAIVE CASE

m_a	$\frac{w_{\max, K_{FF}, FAP}}{w_{\max, naive, FAP}}$	$\frac{w_{\max, K_{FF}, OAP}}{w_{\max, naive, FAP}}$	$\frac{w_{rms, K_{FF}, FAP}}{w_{rms, naive, FAP}}$	$\frac{w_{rms, K_{FF}, OAP}}{w_{rms, naive, FAP}}$
10	0.3513	0.0933	0.22	0.069

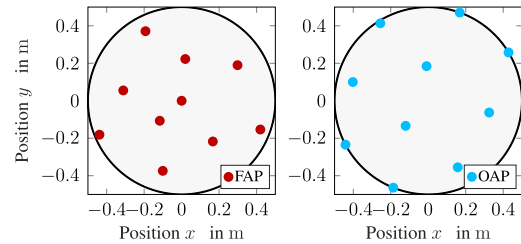


Fig. 9. Actuator positioning based on Fibonacci grid (left) and presented optimization procedure (right).

B. Actuator Placement

Fig. 9 shows the OAP for $m_a = 10$ actuators compared to the Fibonacci positioning. Interestingly, the optimization moved the actuator positions further outward of the center. In particular, the placement on the boundary of the plate is notable. An intuitive choice of the actuator locations would be in the nodal lines of the lower modes such that they do not get excited by the force profile. The resulting quasi-static deformation profile of the optimized actuator location in combination with the optimal mapping $K_{FF}(\theta)$ is shown in Fig. 10. In comparison to Fig. 7, the deformation profile is more flattened and more evenly distributed. Moreover, the excitation of the lower frequent elastic plate modes is clearly reduced and that of the higher frequent ones in the upper third of the model modes is increased (see Fig. 8). This transfers the trend of amplifying higher frequent modes with a higher modal stiffness reducing the quasi-static plate deformation that was also identified in the case of the nonoptimized actuator configuration in conjunction with the optimal mapping $K_{FF}(\theta)$. The trend of amplifying higher frequent modes may arise the question, whether a flat surface profile is paid with the risk of a low amplitude, high-frequent plate vibration. However, with increasing order an excitation of the elastic plate mode requires more energy. In addition, the considered use case is a low-frequent change of motion, which leads to a quasi-static

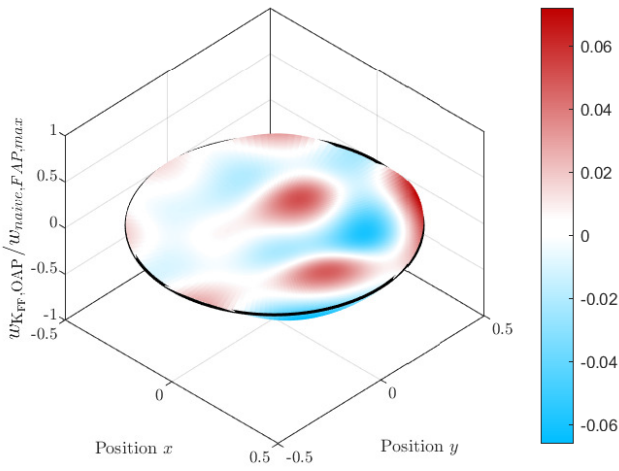


Fig. 10. Normalized plate deformation for optimized actuator placement and optimal force mapping with K_{FF} and ten actuators.

plate deformation and, thus, mitigates the mentioned risk. Furthermore, the peak plate deformation is reduced to 9.33% of the peak deformation in the case of the naive pseudoinverse mapping, as listed in Table I.

C. Number of Actuators

Optimizing the actuator configuration for 3–20 actuators leads to the Pareto front for the rms plate deformation, as shown in Fig. 11. The rms of the plate in a continuous form is given by

$$w_{\text{rms}}^2 = \frac{1}{\pi R^2} \iint_{\mathcal{P}} w^2(r, \varphi) r dr d\varphi \quad (52)$$

$$\stackrel{(37)}{=} \frac{1}{2} \frac{1}{\pi R^2} \mathbf{a}^\top \mathbf{Q} \mathbf{a}.$$

According to (38), the best and worst case rms plate deformation is determined by

$$\sqrt{\frac{1}{2\pi R^2} \lambda_{\min}(\mathbf{Q}(\boldsymbol{\theta})) \|\mathbf{a}\|^2} \leq w_{\text{rms}} \leq \sqrt{\frac{1}{2\pi R^2} \lambda_{\max}(\mathbf{Q}(\boldsymbol{\theta})) \|\mathbf{a}\|^2} \quad (53)$$

on the basis of the given rigid body acceleration in (51) with the Euclidean norm $\|\mathbf{a}\| = \sqrt{3}a_{\text{max}}$. However, the course of the mean deflection is not defined by the mean of the best case and worst case, but by the mean of the projection along the axes of the ellipsoid $\mathbf{Q}(\boldsymbol{\theta})$, i.e., the mean of its trace. Therefore, the course of the mean value does not necessarily lie in the middle of the best case and worst case as it is the case, for three actuators. It is evident to see that an increase in the number of utilized actuators leads to a reduced rms error of the resulting deformation profile of the circular plate. However, a little spike occurs at $m_a = 15$. Since the genetic algorithm explores the feasible set in a stochastic manner, it is possible that the global minimum is not found. Thus, it is likely that the genetic algorithm returned a local minimum for this configuration. An increase of the population size, the number of generations and iterated optimizations, as well as an adapted mutation of the population and selection of individuals may

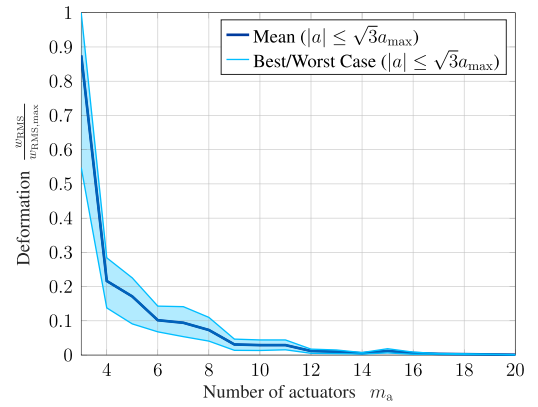


Fig. 11. Course of the rms plate deformation for different numbers of actuators normalized to the largest worst case rms plate deformation.

improve the result but stays in conflict with the computational effort.

D. Optimization Algorithm

In order to evaluate the solutions that are found by the split optimization as presented in Section III-A, we compare it to a direct optimization, i.e., no intermediate optimization of the actuator force profile but the naive solution in the sense of least squares. This leads to the optimization problem

$$\begin{aligned} \min_{\boldsymbol{\theta}} w_1 \max \lambda(\tilde{\mathbf{Q}}(\boldsymbol{\theta})) \\ + w_2 \frac{\sum_{j=1}^{m_o} 1 - r_{\Sigma, j}(\boldsymbol{\theta})}{m_o} + w_3 \Phi(\boldsymbol{\theta}) \\ \text{s.t. } (r_{a, i}, \varphi_{a, i}) \in \tilde{\mathcal{P}} \end{aligned} \quad (54)$$

whereas $\tilde{\mathbf{Q}}(\boldsymbol{\theta})$ is formed by replacing the actuator force \mathbf{u} in (30a) by the least squares solution of (30b). Both problems are optimized with a genetic algorithm, identical in all options as well as the initial condition. The genetic algorithm, mimicking natural biological evolution, is a derivative-free method and domiciled among the metaheuristic optimization algorithms [5]. Based on a random initial population, i.e., test points, the cost function is evaluated. Advancing from here, the next generation of test points is formed by carrying some with low cost in the next generation and mixing as well as randomly modifying the remaining points to create a new set of test points in the following generation.

For each number of actuators, the optimization is repeated ten times to reduce the risk of being stuck in a local minimum. The result is presented in Fig. 12 based on the worst case deformation of each configuration normalized by the solution of the split optimization for three actuators. Despite the optimized configuration of three actuators, all solutions of the split optimization procedure outperform the less sophisticated approach with the actuator profile in the sense of least squares. Moreover, the direct optimization approach does not show a continuous decrease in the worst case performance with an increasing number of actuators. The result is counterintuitive. This indicates that the algorithm could not escape a local minimum. Next, the genetic algorithm is compared with two different optimization algorithms, simulated annealing and pattern search, provided by MATLAB.

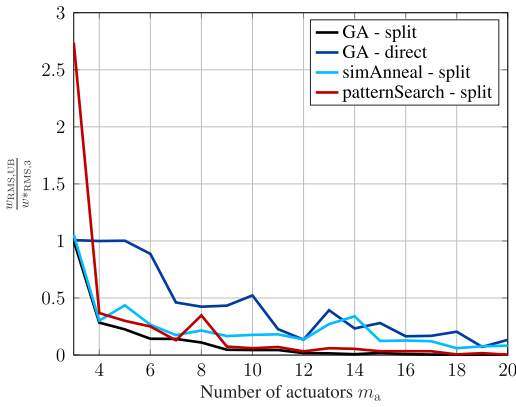


Fig. 12. Comparison of split and direct optimization as well as different algorithms for a split optimization based on the worst case deformation.

Simulated annealing and pattern search are also derivative-free optimization methods. The idea of simulated annealing is minimizing an energy function, defined by the cost function, based on the model of an annealing process [19]. In each step, a random point is evaluated, whereas the probability distribution is scaled by the system's temperature. The temperature is systematically decreased such that the algorithm converges to a minimum. Different from the before mentioned methods, pattern search does not evolve in a random manner but deterministically [25]. Starting from an initial point, the parameter space is searched in each parameter direction, i.e., positive and negative, with a given step size, and the cost function is evaluated at these points. If there exists a point with a lower cost than the initial point, this point becomes the starting point for the next iteration with an increased step size. If the starting point still has the lowest cost, the step size is decreased.

The comparison is conducted with the split optimization to investigate differences in the returned solution. As can be seen in Fig. 12, the simulated annealing algorithm finds for three and four actuators a configuration, which leads to almost the same worst case deformation. However, the third configuration shows a worse deformation than the previous one with less actuators, indicating that the algorithm got stuck in a local minimum. The same arguments hold for 13 and 14 actuators. Opposed to the simulated annealing, the pattern search does not find a solution for three actuators, which is performing similar to the solution of the genetic algorithm. In addition, the algorithm gets stuck in a local minimum for eight actuators. However, for nine and more actuators, the pattern search algorithm returns configurations with a very similar worst case deformation as the results of the genetic algorithm. Nevertheless, no configuration falls below the results of the genetic algorithm, indicating that in general, globally optimal solutions were found.

By having a look at the overall optimization time for each actuator configuration, i.e., the summed time for all ten optimization loops, no significant difference between the split and direct optimization with the genetic algorithm is noticed, see Fig. 13. Both show a slightly increasing time consumption for an increasing number of actuators. Opposed

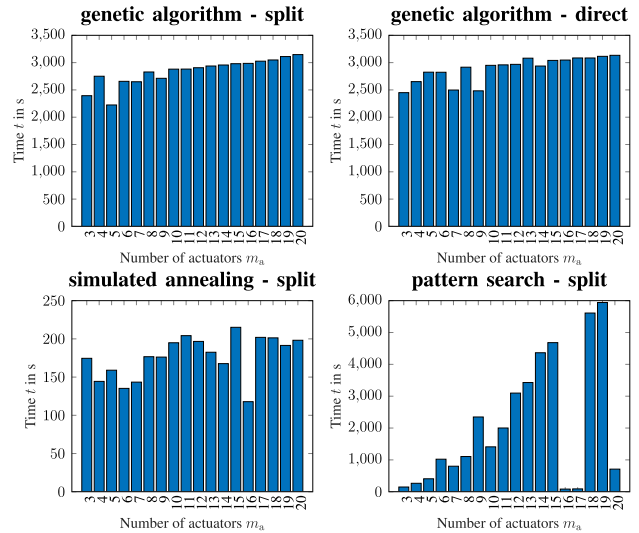


Fig. 13. Time consumption for each actuator over all optimization loops.

to the genetic algorithm, the simulated annealing algorithm returns a solution after a short time duration. However, the quick return of a solution does not compensate the worse worst case deformation. In contrast to the simulated annealing, which has no major time differences between the different number of actuators, the pattern search exhibits a potential increase in the overall optimization time. However, this trend is broken by 16, 17, and 20 actuators. Furthermore, the optimization time with the pattern search for 19 actuators is doubled compared to the genetic algorithm. Since the genetic algorithm with the split optimization leads to the best rms improvements and obtains an almost constant computation time, the genetic algorithm is set to be the best of the considered methods. All conducted optimizations were performed on a personal computer with an i7-10850H processor and MATLAB 2020b.

V. CONCLUSION

In optical systems, the elastic surface deformation of an adjustable optical element due to its motion introduces an aberration of the wavefront. Based on the description of a plate with free boundary, the problem of realizing the demanded motion under minimal surface deflection was encountered. The mapping of the required rigid body acceleration on the actuator force profile as well as the actuator locations were identified as potential measures. In the first step, a closed-form solution for the optimal acceleration mapping onto the force profile for a given set of actuator locations was derived. Here, information about the rigid body modes and elastic modes of the plate is considered to minimize the L_2 -norm of the plate deformation. In a second step, the positioning of the actuators to further reduce the quasi-static plate deformation was developed. The objective to minimize considered the worst case deformation of the plate and additionally took information of the RGA into account, in order to obtain an actuator configuration that evenly addresses the elastic plate deformation. The results show that an OAP in conjunction with an optimal mapping drastically reduces the quasi-static elastic plate deformation in comparison to the use of the

pseudoinverse when only considering information about the rigid body modes. In addition, the trend of exciting higher frequent modes to reduce the elastic deformation profile was identified, too. Moreover, the presented optimization does only require a state-space representation of the system. Hence, our method is also applicable to more complex geometries given as a finite-element model for example.

Upcoming and ongoing investigations will deal with the effect of the quasi-static actuator placement on the controllability of the plate and a minimal number of actuators to stay below a requested maximal plate deformation. This, however, requires a more precise description of the plate, including the additional mass of the actuators, which has been neglected in this work. Moreover, the evaluation of the sensitivity of the plate deformation on the actuator locations is subject of current investigation.

APPENDIX I

Consider the transfer function matrix $\mathbf{G}(s) \in \mathbb{C}^{m \times n}$ from the input $\mathbf{a} \in \mathbb{R}^n$ to the output $\mathbf{y} \in \mathbb{R}^m$. The minimal error

$$\mathbf{e} = \mathbf{y}_d - \mathbf{y} \quad (55)$$

between the desired output \mathbf{y}_d and the plant output \mathbf{y} in the sense of least-squares is obtained by solving

$$\min_{\mathbf{a}} \frac{1}{2} \mathbf{e}^T \mathbf{e} \quad (56a)$$

$$\text{s. t. } \mathbf{y} = \mathbf{G}\mathbf{a}. \quad (56b)$$

Plugging the linear constraint into the objective and solving for its zero-valued derivative lead to

$$\mathbf{a} = \mathbf{G}^+ \mathbf{y}_d. \quad (57)$$

Thus, the minimal error in the sense of least-squares may be expressed through

$$\mathbf{e} = (\mathbf{I} - \mathbf{G}\mathbf{G}^+) \mathbf{y}_d. \quad (58)$$

APPENDIX II

The scaling matrix \mathbf{W} maps the modal rigid body modes \mathbf{q}_r in physically relevant coordinates. In the considered case, \mathbf{W} is defined as follows:

$$\mathbf{W} = \mathbf{q}_r \mapsto \begin{pmatrix} r_z \\ \phi_x \\ \phi_y \end{pmatrix}. \quad (59)$$

Considering rigid body modes that are normalized with respect to the plate surface leads to

$$q_{r_z} = \frac{1}{\underbrace{R\sqrt{\pi}}_{\frac{1}{N_{r_z}}}} r_z \quad (60)$$

for the vertical translation with normalization factor N_{r_z} determined analogously to (18) with mode shape $\psi(r, \varphi) = (1/N_{r_z})$

$$q_{\phi_x} = \frac{2}{\underbrace{R^2\sqrt{\pi}}_{\frac{1}{N_{\phi_x}}}} r \cos \varphi \phi_x \quad (61)$$

for the rotation around the x -axis

$$q_{\phi_y} = \frac{2}{\underbrace{R^2\sqrt{\pi}}_{\frac{1}{N_{\phi_y}}}} r \sin \varphi \phi_y \quad (62)$$

and for the rotation around the y -axis with normalization factors N_{ϕ_x} and N_{ϕ_y} , respectively. Gathering the scaling terms in a diagonal matrix leads to

$$\mathbf{W} = \text{diag}(N_{r_z}, N_{\phi_x}, N_{\phi_y}). \quad (63)$$

REFERENCES

- [1] M. Böhm, M. Glück, A. Keck, J.-U. Pott, and O. Sawodny, "Improving the performance of interferometric imaging through the use of disturbance feedforward," *J. Opt. Soc. Amer. A, Opt. Image Sci.*, vol. 34, no. 5, pp. A10–A21, 2017.
- [2] E. Bristol, "On a new measure of interaction for multivariable process control," *IEEE Trans. Autom. Control*, vol. AC-11, no. 1, pp. 133–134, Jan. 1966.
- [3] J.-W. Chang and C.-C. Yu, "The relative gain for non-square multivariable systems," *Chem. Eng. Sci.*, vol. 45, no. 5, pp. 1309–1323, 1990.
- [4] D. Chhabra, G. Bhushan, and P. Chandna, "Optimal placement of piezoelectric actuators on plate structures for active vibration control via modified control matrix and singular value decomposition approach using modified heuristic genetic algorithm," *Mech. Adv. Mater. Struct.*, vol. 23, no. 3, pp. 272–280, Mar. 2016.
- [5] A. Chipperfield and P. Fleming, "The MATLAB genetic algorithm toolbox," in *Proc. IEE Colloq. Appl. Control Techn. Using MATLAB*, London, U.K., 1995.
- [6] B. Delabre, "Optical design for an adaptive anastigmatic five-mirror extremely large telescope," *Astron. Astrophys.*, vol. 487, no. 1, pp. 389–397, Aug. 2008.
- [7] E. K. Dimitriadis, C. R. Fuller, and C. A. Rogers, "Piezoelectric actuators for distributed vibration excitation of thin plates," *J. Vib. Acoust.*, vol. 113, no. 1, pp. 100–107, Jan. 1991.
- [8] M. Friswell, S. Garvey, J. Penny, and A. Chan, "Selection of control topology for decentralised multi-sensor multi-actuator active control," in *Proc. SPIE*, 1996, pp. 278–284.
- [9] A. Gupta and L. Kumar, "Vibration of non-homogeneous visco-elastic circular plate of linearly varying thickness in steady state temperature field," *J. Theor. Appl. Mech.*, vol. 48, no. 1, pp. 255–266, 2010.
- [10] R. T. Haftka, "Optimum placement of controls for static deformations of space structures," *AIAA J.*, vol. 22, no. 9, pp. 1293–1298, Sep. 1984.
- [11] P. Hickson and R. Racine, "Image quality of liquid-mirror telescopes," *Publications Astron. Soc. Pacific*, vol. 119, no. 854, pp. 456–465, Apr. 2007.
- [12] X. F. Huang, M. Hong, and H. Y. Cui, "The optimal location of piezoelectric sensor/actuator based on adaptive genetic algorithm," in *Applied Mechanics and Materials*, vol. 635. Zürich, Switzerland: Trans Tech Publications, 2014, pp. 799–804.
- [13] H. Jafari, M. Castaño, T. Gustafsson, and G. Nikolakopoulos, "On control structure design for a walking beam furnace," in *Proc. 25th Medit. Conf. Control Autom. (MED)*, Jul. 2017, pp. 1355–1360.
- [14] K. L. Jepsen, L. Hansen, and Z. Yang, "Control pairings of a de-oiling membrane process," *IFAC-PapersOnLine*, vol. 51, no. 8, pp. 126–131, 2018.
- [15] K. R. Kumar and S. Narayanan, "The optimal location of piezoelectric actuators and sensors for vibration of plates," *Smart Mater. Struct.*, vol. 16, no. 6, pp. 2680–2691, Dec. 2007.
- [16] S. Kumar and D. Chhabra, "Optimal placement of piezoelectric actuators on plate structures for active vibration control using genetic algorithm," *Proc. SPIE*, vol. 9057, Mar. 2014, Art. no. 905720.
- [17] F. Peng, A. Ng, and Y.-R. Hu, "Actuator placement optimization and adaptive vibration control of plate smart structures," *J. Intell. Mater. Syst. Struct.*, vol. 16, no. 3, pp. 263–271, Mar. 2005.
- [18] S. S. Rao, T.-S. Pan, and V. B. Venkayya, "Optimal placement of actuators in actively controlled structures using genetic algorithms," *AIAA J.*, vol. 29, no. 6, pp. 942–943, Jun. 1991.
- [19] R. A. Rutenbar, "Simulated annealing algorithms: An overview," *IEEE Circuits Devices Mag.*, vol. 5, no. 1, pp. 19–26, Jan. 1989.
- [20] A. M. Sadri, J. R. Wright, and R. J. Wynne, "Modelling and optimal placement of piezoelectric actuators in isotropic plates using genetic algorithms," *Smart Mater. Struct.*, vol. 8, no. 4, pp. 490–498, Aug. 1999.

- [21] K. Schmidt, F. Beirow, M. Böhm, T. Graf, M. A. Ahmed, and O. Sawodny, "Towards adaptive high-power lasers: Model-based control and disturbance compensation using moving horizon estimators," *Mechatronics*, vol. 71, Nov. 2020, Art. no. 102441.
- [22] J. van Schoot et al., "High-numerical aperture extreme ultraviolet scanner for 8-nm lithography and beyond," *Proc. SPIE*, vol. 16, no. 4, 2017, Art. no. 041010.
- [23] R. Swinbank and R. J. Purser, "Fibonacci grids: A novel approach to global modelling," *Quart. J. Roy. Meteorol. Soc., J. Atmos. Sci., Appl. Meteorol. Phys. Oceanogr.*, vol. 132, no. 619, pp. 1769–1793, Jul. 2006.
- [24] S. Timoshenko and S. Woinowsky-Krieger, *Theory of Plates and Shells*. New York, NY, USA: McGraw-Hill, 1959.
- [25] V. Torczon, "On the convergence of pattern search algorithms," *SIAM J. Optim.*, vol. 7, no. 1, pp. 1–25, Feb. 1997.
- [26] S. Treiber, "Multivariable control of non-square systems," *Ind. Eng. Chem. Process Des. Develop.*, vol. 23, no. 4, pp. 854–857, Oct. 1984.
- [27] J. Uhlmann, "On the relative gain array (RGA) with singular and rectangular matrices," *Appl. Math. Lett.*, vol. 93, pp. 52–57, Jul. 2019.
- [28] J. L. Wagner, K. Schmidt, M. Böhm, and O. Sawodny, "Optimal actuator placement and static load compensation for Euler–Bernoulli beams with spatially distributed inputs," *IFAC-PapersOnLine*, vol. 52, no. 15, pp. 489–494, 2019.
- [29] A. Zagrai and D. Donskoy, "A 'soft table' for the natural frequencies and modal parameters of uniform circular plates with elastic edge support," *J. Sound Vib.*, vol. 287, pp. 343–351, Oct. 2005.



André Heining received the B.Sc. degree in mechanical engineering from the University of Paderborn, Paderborn, Germany, in 2018, and the M.Sc. degree in engineering cybernetics from the University of Stuttgart, Stuttgart, Germany, in 2021.

Since 2021, he has been with the Institute for System Dynamics, University of Stuttgart, as a Research Assistant. His research interests include modeling and control of distributed systems.



Kevin Schmidt received the Ph.D. degree in engineering cybernetics from the Institute for System Dynamics, University of Stuttgart, Stuttgart, Germany, in 2020. His dissertation focused on disturbance compensation for adaptive high-power lasers with deformable mirrors.

He was with the Cymer Center for Control Systems and Dynamics, University of California at San Diego, La Jolla, CA, USA, in 2016. Since 2021, he has been with the Corporate Sector Research and Advanced Engineering, Robert Bosch GmbH, Renningen. His research interests include modeling, optimization, and control of distributed systems and uncertainty quantification, and applications in the field of networked and cyber-physical systems.



Ulrich Schönhoff graduated in electrical engineering from the University of Hannover, Hanover, Germany, in 1995. He received the Ph.D. degree in mechanical engineering from the Darmstadt University of Technology, Darmstadt, Germany, in 2002.

Since 2003, he has been with Carl Zeiss SMT GmbH, Oberkochen, Germany, a leading manufacturer of precision optics, where he is currently a Principal Engineer. He is active in mechatronics development. His focus is on dynamics and control.



Oliver Sawodny (Senior Member, IEEE) received the Dipl.Ing. degree in electrical engineering from the University of Karlsruhe, Karlsruhe, Germany, in 1991, and the Ph.D. degree from Ulm University, Ulm, Germany, in 1996.

In 2002, he became a Full Professor at the Technical University of Ilmenau, Ilmenau, Germany. Since 2005, he has been the Director of the Institute for System Dynamics, University of Stuttgart, Stuttgart, Germany. His current research interests include methods of differential geometry, trajectory generation, and applications to mechatronic systems.